Received: 21 June 2021 | Revised: 14 October 2021 | Accepted: 4 December 2021

DOI: 10.1111/jace.18294

Journal of the American Ceramic Society

RESEARCH ARTICLE

Crystal chemistry and ion-irradiation resistance of Ln_2ZrO_5 compounds with Ln = Sm, Eu, Gd, and Tb

Robert D. Aughterson | **Gregory R. Lumpkin** | **Zhaoming Zhang** | **Maxim Avdeev** | **Linggen Kong**

Australian Nuclear Science and Technology Organisation, Lucas Heights, New South Wales, Australia

Correspondence
Linggen Kong, Australian Nuclear Science and Technology Organisation, Locked Bag 2001, Kirrawee DC, NSW 2232, Australia.
Email: lnk@ansto.gov.au

Abstract

The previously unattained fabrication of single phase Ln_2ZrO_5 (Ln = Sm, Eu, Gd, and Tb) compounds via relatively low sintering temperature (1400°C) is achieved in this study using a coprecipitation method. The crystal structures have been investigated by neutron, synchrotron X-ray powder diffraction, and electron diffraction techniques. While the general long-range structure may be well described by the defect-fluorite type structure with $Fm\bar{3}m$ symmetry, electron diffraction has highlighted a complex underlying modulated structure that varies between each compound. These compounds have been tested for ion-irradiation response using in situ 1 MeV krypton ions and transmission electron microscopy characterization. None of the compounds undergo a crystalline to amorphous transition, even holding at 50 K. Both the underlying fluorite and modulated superstructures are little affected by the irradiation. However, some atomic rearrangements are observed in the postirradiated electron diffraction patterns for the Sm_2ZrO_5 specimen.

KEYWORDS

ion-irradiation, lanthanide zirconate, Ln_2ZrO_5, microstructure analyses, soft chemistry synthesis

1 | INTRODUCTION

With the ongoing development of refractory ceramic compounds, designed for use within high energy particle, corrosive, and ablative environments, zirconates have been developed due to their suitable properties. Rare-earth zirconate compounds possessing a fluorite or pyrochlore crystal structure and having different stoichiometries are of interest for numerous applications, including nuclear fuel and related materials[1,2], nuclear waste forms,[3–8] fast ion conductors,[9–11] and thermal barrier coatings,[12–14] among others.[15,16] Possessing remarkable properties such as high radiation tolerance, high chemical durability, and ability to incorporate a range of actinides into the structure, rare-earth zirconates with stoichiometry $A_2Zr_2O_7$ have been studied as potential ceramic materials for inert matrix fuel (IMF)[17,18] using MgO as a secondary phase to improve thermal conductivity.[19] Furthermore, ceramic-based waste-forms offer a containment matrix for radio-toxic elements produced as a byproduct of spent nuclear fuel or from decommissioning nuclear-based weapons. The ability of zirconate compounds to incorporate high actinide loadings[3,19] along with their high radiation tolerance,[6,20] and generally improved aqueous durability relative to titanate-based ceramics, has made these compounds the focus of waste-form-related studies.

Studies on Ln_2O_3–ZrO_2 systems (Ln = lanthanides) show regions of single-phase solid solutions between

stoichiometries of $Ln_{0.25}Zr_{0.75}O_{1.88}$ through to Ln_2ZrO_5.[21–23] However, these solid solutions only exist for limited lanthanides, predominantly for Ln = Sm–Dy. Attempts to fabricate smaller, heavier lanthanide zirconates in the Ln_2ZrO_5 region tend to give multi-phase materials such as Yb_2O_3 solid solution coupled with the delta-phase $Yb_4Zr_3O_{12}$.[24,25] For the lighter, larger lanthanides (Ln = La, Pr, Nd), a pyrochlore plus cubic solid solution tends to form.[25–27] There has only been limited study on zirconate compounds of stoichiometry Ln_2ZrO_5. An X-ray and electron diffraction study on Ln_2O_3-ZrO_2 compounds by Withers et al.[22] gave some insight into the complexity of the crystal structures of several Ln_2ZrO_5 (Ln = Sm, Gd, Tb, Dy) compounds. These structures tended to present as either fluorite-like or pyrochlore-like with diffuse features found within the electron diffraction patterns showing the presence of modulated structure. The temperature–structure study on Gd_2ZrO_5 carried out by Lyashenko et al.[28] showed at lower temperature, a defect fluorite structure containing –OH groups was formed. At temperatures above approximately 1000°C, the –OH groups were driven off, and two commensurate defect-fluorite phases were formed with a small volume of ordered phase within the larger fluorite type phase. This type of observation has been noted in several studies on related cubic rare-earth titanates of the same stoichiometry Ln_2TiO_5 where nano-domains of pyrochlore-type structure exist within a defect-fluorite-like matrix.[29–32]

Starting with the basic fluorite structure, $^{VIII}M^{IV}X_2$, where M can be a range of medium to large tetravalent cations (e.g., Zr, Hf, Th, U) or divalent cations (e.g., Ca, Sr, Ba) in eightfold coordination, and X is typically O^{2-} or F^- in fourfold coordination, there are many variations on the theme when considering charge balanced combinations of cations and anions. These structures exist in cubic space group $Fm\bar{3}m$, and when there is more than one cation present, they are generally disordered over the available cation sites. However, in many compositions, electron diffraction patterns reveal the structures also include one or more modulations on the parent fluorite structure.[22]

Ordered derivatives of the fluorite structure are also common, including compounds with the $A_2B_2O_7$ pyrochlore ("227" type)[33–36] structure which adopts space group $Fd\bar{3}m$, the A_3BO_7 ("317" type), and the A_2BO_5 ("215" type) compounds.[22,25] Literally speaking, in these broad families, there are hundreds of known compounds, providing a fertile ground for discovery research in phase transitions and useful industrial properties.

With focus on nuclear materials, radiation tolerance studies have been a common theme for pyrochlore- and fluorite-structured materials. Studies by Lumpkin et al.[37–39] collated the available radiation tolerance data on the $Ln_2B_2O_7$ (B = Ti, Zr, Hf, Nb, Ta, Sn) pyrochlore–fluorite system. There was a general trend of improved radiation tolerance, ability to maintain the crystalline structure during irradiation, found for those compounds with fluorite structure with the zirconates showing the best response of those surveyed. In an oxide pyrochlore review by Subramanian et al.,[40] an empirically derived stability field for pyrochlore formation was established based on the A^{3+} to B^{4+} cation ionic radii ratios. This pyrochlore stability field ranges from r_{Gd}/r_{Zr} = 1.46 to r_{Sm}/r_{Ti} = 1.78. From this, $Ln_2Zr_2O_7$ compounds with Ln = La, Ce, Pr, Nd, Pm, and Gd can reasonably be expected to form the pyrochlore structure, while zirconates with lanthanides smaller than Gd will tend to form the fluorite structure. For $Ln_2Ti_2O_7$ pyrochlore compounds, smaller lanthanides tend to give improved radiation response[41] due to their increased tendency for an irradiation-induced order to disorder transition. Further improvements in ion-irradiation tolerance have been noted for the cubic Ln_2TiO_5 when compared with the related $Ln_2Ti_2O_7$ compounds due to greater level of disorder found in the former.[42] It is this ability for the cubic structure to maintain crystallinity in a disordered state that has often been correlated with the rare-earth zirconates' outstanding radiation tolerance.[43,44]

A 2 MeV Au ion-irradiation study by Begg et al.[6] on the $Gd_2(Ti_{2-x}Zr_x)O_7$ system of compounds showed both a systematic increase in fluorite-like disorder and improved resistance to radiation-induced amorphization with increasing zirconium content. As with previous radiation studies on the $Gd_2Zr_2O_7$ compound ion-irradiation helped transition the crystal structure from pyrochlore to defect fluorite but did not amorphize the structure.[20] In fact the only zirconate in the $Ln_2Zr_2O_7$ series, which undergoes heavy ion-irradiation-induced amorphization in the low MeV energy range, is $La_2Zr_2O_7$ by 1.5 MeV Xe ions.[16] This compound did however have a low critical temperature of 310 K above which crystallinity could be maintained during ion irradiation.

In the present study, a soft coprecipitation synthesis method has been employed to ensure the complete mixing of the reactants, thus resulting in high composition homogeneity of the product. The Ln_2ZrO_5 materials have been characterized by neutron and synchrotron X-ray powder diffraction, and electron microscopy to understand the nature of the average and local structure and the phase transition from pyrochlore to defect fluorite as a function of the decreasing ionic radius of the A-site cation. An important question to be addressed here is the effect of the size of lanthanide on the order-disorder transformation in the Ln_2ZrO_5 system. As the pyrochlore to defect fluorite transformation is well known in the $Ln_2B_2O_7$ compounds, a major aspect of this study will be to examine our new results in the light of the differences in stoichiometry between the two systems. The experimentally

determined crystal structural characteristics are coupled with the property of radiation tolerance to give fundamental understanding between these. The results and trends may be used to guide decisions on applications of zirconates in extreme environments.

2 | EXPERIMENTAL

2.1 | Materials and methods

Lanthanide(III) nitrate hydrate [$Ln(NO_3)_3{\cdot}xH_2O$] (99.9%+) (Ln = Sm, Eu, Gd, or Tb) and zirconyl nitrate hydrate [$ZrO(NO_3)_2{\cdot}xH_2O$] (99+%) were purchased from Sigma-Aldrich with the Zr content quantitatively determined by gravimetric analyses. All chemicals were A. R. grade and used as received. Milli-Q grade water was used in all experimental procedures.

The calculated amounts of lanthanide nitrate and zirconyl nitrate were dissolved in 100 ml of water. The mixture was magnetically stirred to produce an aqueous solution. Note that 1.667 M ammonia solution was dropwise added to form the precipitates until the ammonia concentration reaches 0.1 M with pH = ~ 11.1. The resultant precipitate was further stirred for 1 h and separated from the aqueous phase by centrifuge for 20 min at 9500 rpm, dried overnight in a 95°C oven, and then calcined for 4 h at 750°C in a furnace in air with ramp rate of 2°C/min. The calcined powder was pelletized using a uniaxial cold press at approximately 180 MPa and sintered for 24 h at 1400°C in air with 5°C/min heating/cooling rate. The supernatant of the centrifugation was collected and dried at 100°C. No solid materials were detected by thermogravimetric analysis at 750°C, which confirmed that no metal ions were lost during centrifuge processing.

A further bulk polycrystalline Sm_2ZrO_5 sample was synthesized via the conventional mixed oxide route. Preheated at 800°C for 4 h and stoichiometric quantities of the precursor oxides Sm_2O_3 and TiO_2 (Sigma-Aldrich, 99.9 %+) were weighed and ball-milled using yttria-stabilized ZrO_2 balls carried out in cyclohexane media. The pellets were consolidated by uniaxial pressing followed by cold isostatic pressing at 250 MPa. Sintering was carried out at 1500°C for 48 h in air using a heating and cooling rate of 5°C/min.

2.2 | Characterization

Scanning electron microscopy (SEM): Fragments of samples were mounted in epoxy resin and polished using several grades of diamond polish down to a final 1-μm diamond finish. SEM was carried out on a Zeiss Ultra Plus operated at accelerating voltage 15 kV with the morphology analyzed by annular selected backscattered imaging.

Synchrotron X-ray diffraction (SXRD): The crystal structure data for Sm_2ZrO_5, Eu_2ZrO_5, and Gd_2ZrO_5 were collected using the Australian synchrotron 10-BM-1 powder diffraction beamline[45] fitted with a Mythen II microstrip detector. The wavelength was determined as 0.72749 Å using an NIST LaB_6 (660b) standard for wavelength calibration. Data were collected at room temperature between 10–80° 2-theta, for 5 min at each of the two detector positions of Mythen detector and binned in steps of 0.00375°. The diffraction data were refined via the Rietveld method using software Rietica.[46] Background was corrected for via user-input points, thermal parameters set to isotropic, and peaks were fitted via the pseudo-Voigt profile function.

Neutron diffraction: The Echidna, high resolution, powder diffraction beamline at the Australian Nuclear Science and Technology Organisation (ANSTO)[47] was used for collection of neutron diffraction data for the Tb_2ZrO_5 sample. The powdered specimen was held within a vanadium cylinder, and data were collected at room temperature. The neutron wavelength was 1.62150 Å. As with the synchrotron diffraction data, the diffraction data were refined using the Rietveld method.

Transmission electron microscopy (TEM): Selected samples were investigated using a JEOL 2200 FS TEM equipped with an in-column Omega energy filter and an Oxford X-Max energy-dispersive X-ray detector (EDS) analytical system. The TEM was operated at the maximum accelerating potential of 200 kV. Samples were prepared by crushing small pieces of the ceramics under ethanol using an agate mortar and pestle and depositing a small drop of the solution onto holey carbon grids. EDS spectra were obtained from suitably thin grains, at least 30 grains per sample, to ensure that sample compositions are within specification with regard to Ln_2ZrO_5 stoichiometry and free of impurities. The EDS system was standardized using the Cliff-Lorimer k-factor method.[48] Unfiltered selected area electron diffraction pattern (SAED) was recorded digitally from thin areas of these grains after tilting into zone axis orientations with the main objective being the identification of diffuse scattering features. The SAEDs were measured and indexed using the Gatan Microscopy Suite (GMS3) and Crystal Maker software (Crystal Maker and Crystal Diffract).

In situ irradiation coupled with TEM characterization: The TEM specimens were prepared as finely ground crystals as described in the TEM methods section. Note that 1 MeV Kr ion-irradiation was carried out along with in situ TEM characterization using Hitachi H-9000-NAR operated at 300 kV, at the Argonne national laboratory.[49] For each irradiation experiment five electron transparent crystals were selected and monitored via collection of bright

field images and electron diffraction patterns. The specimens were monitored at a range of fluence steps to track any crystal structure changes associated with increasing fluence. The irradiation and monitoring were kept separate to eliminate any potential synergistic annealing caused by both ion-beam and electron-beam irradiating the specimen at the same time. The Sm_2ZrO_5 specimen was held at 50 K during irradiation, while all other samples were held at room temperature.

Density and apparent porosity: Archimedes' displacement method was employed to determine the pelletized sample density using water as the medium. Bulk density refers to the ratio of the mass of a material to its bulk volume. Apparent porosity refers to the percentage ratio of the volume of the open pores in a material to the bulk volume of that material. The theoretical density was determined from the structural parameters, which were determined via the Rietveld refinement method using the software Rietica.[46]

3 | RESULTS AND DISCUSSION

3.1 | Fabrication

A comparison of the differences in morphology for the Sm_2ZrO_5 compound achieved via two different fabrication approaches are shown in Figure 1. These images were collected using backscattered SEM imaging, an approach useful for highlighting any variation in the distribution of elements within the sampled area. Figure 1A is the Sm_2ZrO_5 sample fabricated in the present study, while Figure 1B is the Sm_2ZrO_5 sample produced using the conventional mixed oxide route for a solid state reaction, with the detailed method disclosed previously.[25] These two samples appear distinctly different; there is much greater porosity in the mixed oxide route fabricated sample, and there is also poorer homogeneity indicated via variation in the intensity of grey-scale in this sample relative to the wet-chemistry approach. Previous studies have shown that improved mixing at the molecular level is achieved via this wet-chemistry approach leading to improved homogeneity.[19,50] The software ImageJ[51] was utilized to investigate the porosity of the SEM backscattered images for Figure 1, where the measured porosities were 15.6% and 27% for the wet-chemistry and mixed oxide route respectively (Figures S2-S3 at SM). While there may be some variation in calculated values for porosity depending on the image contrast thresholding used, this source of error should be consistent if the same approach is used for each image. The greater porosity evident for the mixed oxide route fabricated sample may be attributed to the much greater particle size for the precursor oxide powders

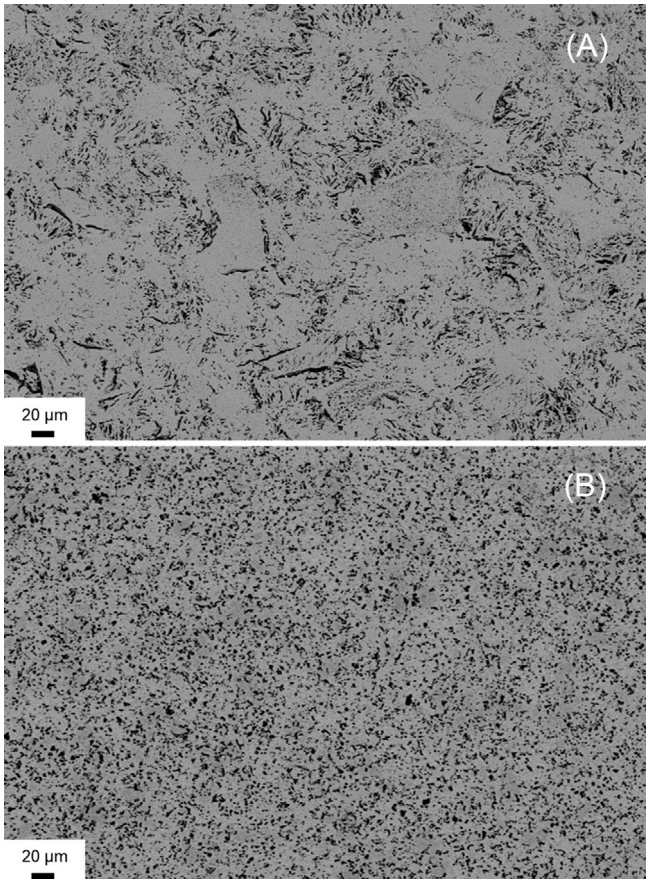

FIGURE 1 Scanning electron microscopy (SEM) annular selected backscattered images of Sm_2ZrO_5 fabricated via (A) soft-chemistry route and (B) conventional mixed oxide route. The black regions are pores, while slight variation in the grey contrast (image-B) is indicative of slight variation in elemental distribution

when compared with those of the molecular level mixing achieved via the wet-chemistry approach.

An initial attempt was made to fabricate a large portion of the lanthanides, from lanthanum to ytterbium, in the Ln_2ZrO_5 stoichiometry as single-phase materials. This proved to be successful for four of the lanthanides, Sm, Eu, Gd, and Tb, while the remaining all consisted of multiple phases as shown in Figure S1 at Supporting Materials (SM). The series of backscattered images shown in Figure 2 is of the successful attempts. Based on SEM analysis of the four, single-phase Ln_2ZrO_5 compounds studied here (Ln = Sm, Eu, Gd, Tb), there was almost complete reaction of all precursors after sintering in air at 1400°C for 24 h. Small amounts, less than 1 vol%, of Ln_2O_3 (Sm, Eu or Gd) precursors were detected in each respective lanthanide zirconate, while no precursor was detected in the Tb_2ZrO_5 sample. Furthermore TEM–EDS analysis was utilized to confirm the homogeneous nature of the fabricated compounds and to quantify the cation ratios. The TEM–EDS system had previously been calibrated

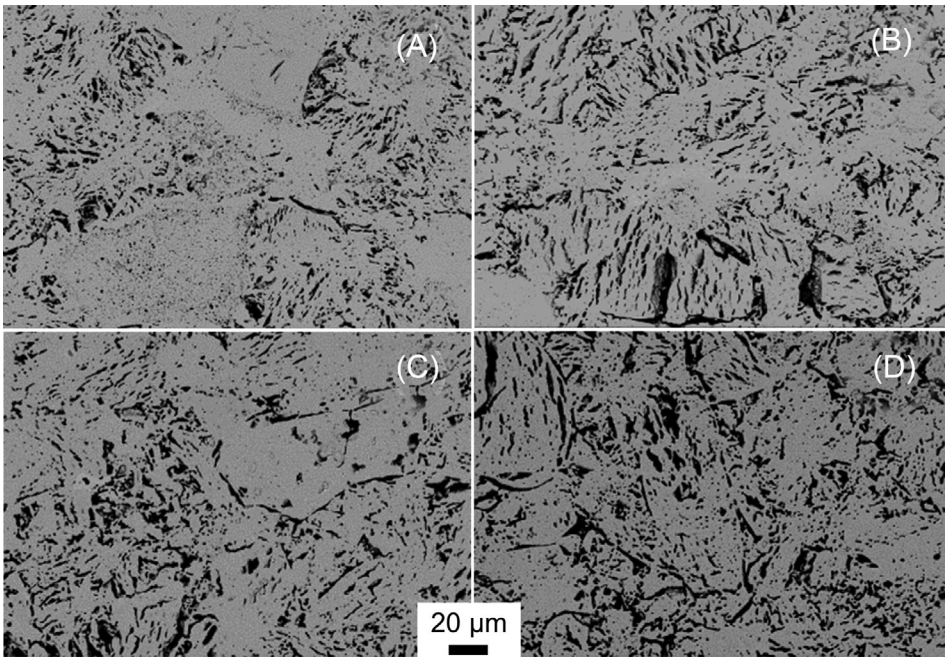

FIGURE 2 Scanning electron microscopy (SEM) annular selective backscattered images for compounds of (A) Sm_2ZrO_5, (B) Eu_2ZrO_5, (C) Gd_2ZrO_5, and (D) Tb_2ZrO_5. Black regions are pores

with numerous titanate-based compounds, including rare-earth pyrochlores and zirconolites, via the Cliff-Lorimer k-factor method.[48] By analyzing 30 grains for each specimen, a good level of statistical confidence is achieved (Tables S1–S4 at SM). The calculated cation and anion numbers, $Sm_{2.00(0.08)}Zr_{0.97(0.06)}O_{4.94(0.001)}$, $Eu_{2.00(0.04)}Zr_{0.93(0.04)}O_{4.86(0.01)}$, $Gd_{2.00(0.06)}Zr_{0.92(0.05)}O_{4.84(0.01)}$, and $Tb_{2.00(0.07)}Zr_{1.05(0.06)}O_{5.10(0.01)}$, with errors based on two standard deviations, shown in brackets, indicate the homogeneous nature of each sample. This result is significant as zirconates tend to require higher sintering temperatures and long sintering times to achieve a reasonable percentage of reaction between the precursors. A review of the Ln_2O_3–ZrO_2 systems by Andrievskaya[27] showed that it was possible to achieve solid solutions for compositions between $Ln_2Zr_2O_7$ to Ln_2ZrO_5 where Ln = Sm, Eu, Gd and Tb, although the phase diagrams tended to start at temperatures of 1800°C and above. Studies on rare-earth oxide–zirconia solid solutions are rarely conducted below 1500°C due to low diffusion mobility plus a slow rate of solid solution formation.[27]

3.2 | Crystal structure

While in this study ideally all samples would have been characterized via neutron diffraction, the large neutron absorption cross-sections for the lanthanides Sm, Eu, and Gd have made this impractical. In this study, Tb_2ZrO_5 has been analyzed via neutron diffraction (Figure 3). The structure has been identified as a defect fluorite with $Fm\bar{3}m$ symmetry. This was as expected as there is a large solid solution of fluorite-related structure for the Tb_2ZrO_5 to $Tb_2Zr_2O_7$, and higher zirconia content, region.[22] The oxygen occupancy, determined from Rietveld refinement of the data, of 87% ± 1% (Table 1), is slightly higher than that expected (83 %) for the nominal stoichiometry Tb_2ZrO_5 and idealized oxidation states of Tb^{3+}, Zr^{4+}, and O^{2-}. Due to the lower sensitivity of X-rays to oxygens (especially in the presence of much heavier lanthanides), the oxygen occupancy was fixed to the nominal 83% in the refinements against SXRD data for Ln_2ZrO_5 (Ln = Sm, Eu, and Gd), although Sm, Eu, and Gd are all expected to be trivalent.

While it was expected that the smaller lanthanide Tb would take on a fluorite-type structure for the solid solution between Tb_2ZrO_5 and $Tb_2Zr_2O_7$, it was not known if the larger lanthanide Sm would take on a pyrochlore-type structure, especially when sintered at the relatively lower temperature of 1400°C. Based on the cation ratios of Ln: Zr, it is expected that $Gd_2Zr_2O_7$ (r_{Gd3+}/r_{Zr4+} = 1.46) would be on the phase boundary between pyrochlore and defect-fluorite, while smaller lanthanides such as Tb to Lu would assume the defect-fluorite structure regardless of sintering temperature.[40] For $Gd_2Zr_2O_7$, the phase transition temperature boundary from pyrochlore to defect-fluorite is 1530°C, for $Sm_2Zr_2O_7$, this transition is achieved at 2000°C,[52] while for $Eu_2Zr_2O_7$ at 1855°C.[53] However, in a phase diagram for the Ln_2O_3–ZrO_2 system by Tabira et al.,[23] it was indicated that Sm_2ZrO_5 and Gd_2ZrO_5 sintered at 1500–1600°C could be found in the

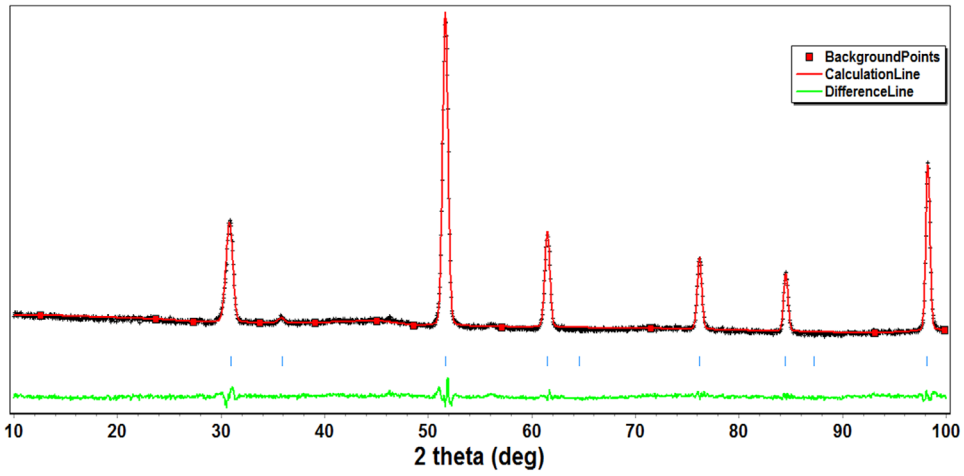

FIGURE 3 Neutron diffraction data with Rietveld calculated fit for Tb_2ZrO_5. The black crosses show the measured diffraction data, the red trace is the calculated fit with the difference between measured and calculated displayed by the green line below the diffraction pattern. The blue markers indicate the diffraction maxima positions expected in the $Fm\bar{3}m$ structure

TABLE 1 Rietveld refinement details from powder SXRD data (Sm_2ZrO_5, Eu_2ZrO_5, and Gd_2ZrO_5), and neutron diffraction data for the Tb_2ZrO_5 compound. The fits are based on Fm$\bar{3}$m symmetry. Oxygen occupancies were fixed for X-ray refinements based on the Ln^{3+} and Zr^{4+} oxidation states

	Lattice parameter (Å)	Oxygen occupancy	U*100 (*Ln*/Zr)	U*100 (O)	Rp (%)	χ^2	Rwp (%)
Sm_2ZrO_5	5.35795(1)	0.83	2.74(1)	7.40(8)	4.14	9.86	5.07
Eu_2ZrO_5	5.33825(2)	0.83	2.84(1)	7.48(7)	3.66	7.72	4.59
Gd_2ZrO_5	5.319573(5)	0.83	2.73(1)	7.1(1)	3.97	10.13	5.67
Tb_2ZrO_5	5.25437(5)	0.87(1)	2.28(7)	4.6(1)	3.68	2.30	4.70

Rp, unweighted profile R-factor; Rwp, weighted profile R-factor.

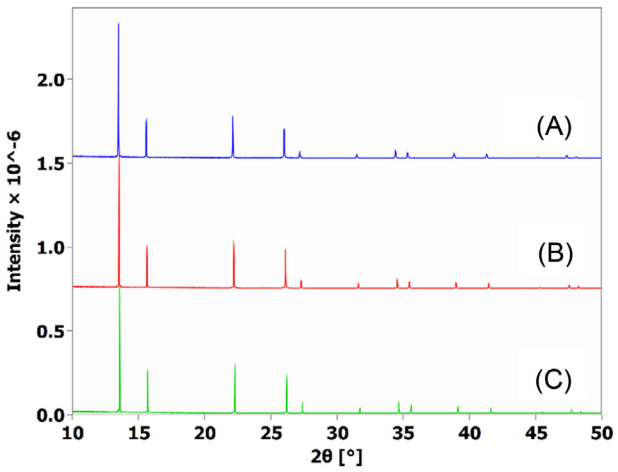

FIGURE 4 Synchrotron powder X-ray diffraction patterns for samples (A) Sm_2ZrO_5, (b) Eu_2ZrO_5, (C) Gd_2ZrO_5. Patterns are offset for clarity. Diffraction maxima match those for the fluorite structure, $Fm\bar{3}m$ symmetry

defect-fluorite type structure. The synchrotron powder X-ray diffraction data (Figure 4) from our study show a defect-fluorite-type structure with $Fm\bar{3}m$ symmetry.

TABLE 2 Density and apparent porosity for the Ln_2ZrO_5 compounds

	Density (calculated) (g/cm^3)	Density (measured) (g/cm^3)	Apparent porosity (%)
Sm_2ZrO_5	6.77	5.85	13.6
Eu_2ZrO_5	6.82	5.76	15.5
Gd_2ZrO_5	6.97	5.90	15.4
Tb_2ZrO_5	7.07	6.17	12.7

The presence of sharp peaks and absence of any broad features within the diffraction patterns are indicative of a highly crystalline, single-phase structure for each of the compounds studied. There is a small shift in diffraction maxima locations to higher angles that correlates with the reduction in lanthanide size, from Sm, Eu to Gd. This corresponds to a reduction in lattice parameter from Sm_2ZrO_5 to Tb_2ZrO_5 (Table 1) with the smallest lanthanide, Tb, from our investigated series having the smallest cell parameter.

The porosity of these compounds (Table 2) was estimated from the theoretical density, calculated from

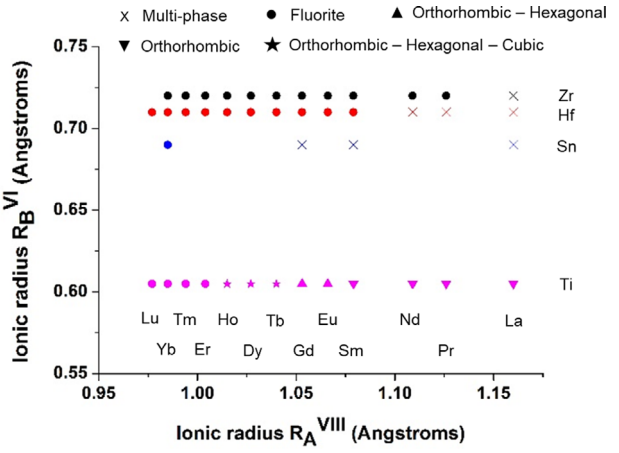

FIGURE 5 The major phases formed for various rare-earth/metal oxide combinations with the stoichiometry Ln_2BO_5 (Ln = lanthanides, B = Ti, Sn, Hf, and Zr)

molecular weight and cell volumes from crystal structure refinements (Table 1), and the measured density. The relatively high porosity determined in this study is significant, as it would detrimentally affect the potential of these materials used in nuclear applications, either by increasing the waste volume in nuclear waste form applications, or by lowering the thermal conductivity in IMF applications. A reduction in porosity might be achieved via higher temperature sintering, the use of pressure such as hot isostatic pressing, or the addition of a secondary phase such as magnesium oxide.

Figure 5 lists all the phases formed for different combination of lanthanides and group IV metals with the stoichiometry Ln_2BO_5 (B = Ti, Zr, Hf, and Sn), from this study as well as previous studies.[22,25,29,32,54–60] While the present study has focused on the relatively low temperature sintering at 1400°C, previous studies have shown that it is possible to achieve limited solid solutions between $Ln_2Zr_2O_7$ and Ln_2ZrO_5 for a wide variety of lanthanides including Pr_2ZrO_5 through to Yb_2ZrO_5[54] including the compositions studied here. However, sintering temperature of 1800–2200°C had to be employed to achieve these single-phase compounds. Many of these Ln_2ZrO_5 compounds were previously described as either defect-fluorite in $Fm\bar{3}m$ symmetry, or for the smaller lanthanides defect fluorite compounds with the related C-type bixbyite with cubic Ia-3 symmetry. All four compounds in the current study, Ln_2ZrO_5 (Ln = Sm, Eu, Gd, and Tb), can be described satisfactorily based on the fluorite structure. In a study on the Eu_2O_3–ZrO_2 system by Lopato et al.[55] where lower sintering temperature (1250°C) was employed, the Eu_2ZrO_5 was also described as a defect fluorite structure. It should be noted however that a previous study on Ln_2ZrO_5 by Withers et al.[22] cautioned that describing these structures simply as defect fluorite could be misleading as they also tend to possess highly complex modulated local structures.

Figure 5 also includes other, previously fabricated rare-earth zirconates with the Ln_2BO_5 stoichiometry; Pr_2ZrO_5 and Nd_2ZrO_5 (sintered at and above 2200 and 2000°C, respectively),[54] Dy_2ZrO_5,[22] Ho_2ZrO_5,[54] Er_2ZrO_5,[56] and Yb_2ZrO_5[54] (all sintered ≥1600°C). The similar chemistry and ionic size of hafnium relative to zirconium has resulted in similar combinations of the rare-earths and metal oxides forming the fluorite type structure for the Ln_2BO_5 stoichiometry (Figure 5). The Ln_2HfO_5 stoichiometry could not be achieved for Ln = La, Pr, and Nd[59]; however for the remainder of the rare-earth elements single-phase compounds could be formed (Ln = Sm–Dy[58], Ho–Lu[57]). The use of cation size ratios to predict phase stability ranges for the pyrochlore and defect-fluorite phases for the $Ln_2B_2O_7$ stoichiometry in previous studies has proven to be a good guide; however this appears to break down when looking at Ln_2BO_5 stannates (Figure 5). The formation of only Yb_2SnO_5 in the stannate system[25] indicates a significant variation in chemistry from tin when compared with hafnium or zirconium. Finally, the significantly smaller ionic size of Ti has resulted in regions where rare-earth titanates can take on multiple structures.[60] It is only the smaller lanthanides (terbium to lutetium) where the Ln_2TiO_5 stoichiometry can take on the cubic form. These cubic rare-earth titanates have been described as long-range fluorite with short-range domains of pyrochlore structure.[29,32]

While the long-range average crystal structure can be well defined as having the defect-fluorite structure based on our X-ray and neutron diffraction results, TEM studies employing electron diffraction show complex modulations. In the ⟨111⟩ zone, the electron diffraction results for the four compounds (Figure 6) show a systematic change from Sm_2ZrO_5 to Eu_2ZrO_5, Gd_2ZrO_5, and Tb_2ZrO_5. Sm_2ZrO_5 (Figure 6A) has diffuse features similar to those reported previously for $Yb_2Sn_{1.25}O_{5.5}$.[25] The extra scattering generally consists of sets of six ball-and-stick features around the main Bragg beams with sets of three diffuse spots arranged in triangles in between them. The scattering is relatively weak for Sm_2ZrO_5, but the relationship between the extra spots and Bragg spots can be determined to be 0.21(220)*. The example shown here for Eu_2ZrO_5 has similar, but stronger scattering features described using the modulation wave approach as 0.23 (220)*. The superlattice of Gd_2ZrO_5 is commensurate with the underlying fluorite lattice in the ⟨111⟩ zone axis, and the extra spots are sharp and evenly spaced according to the wave vector 0.25 (220)*. There are no obvious extra spots or reasonably intense diffuse features present in the ⟨111⟩ zone axis orientation (Figure 6D) for Tb_2ZrO_5 sample. This is consistent with previous work on the "227"

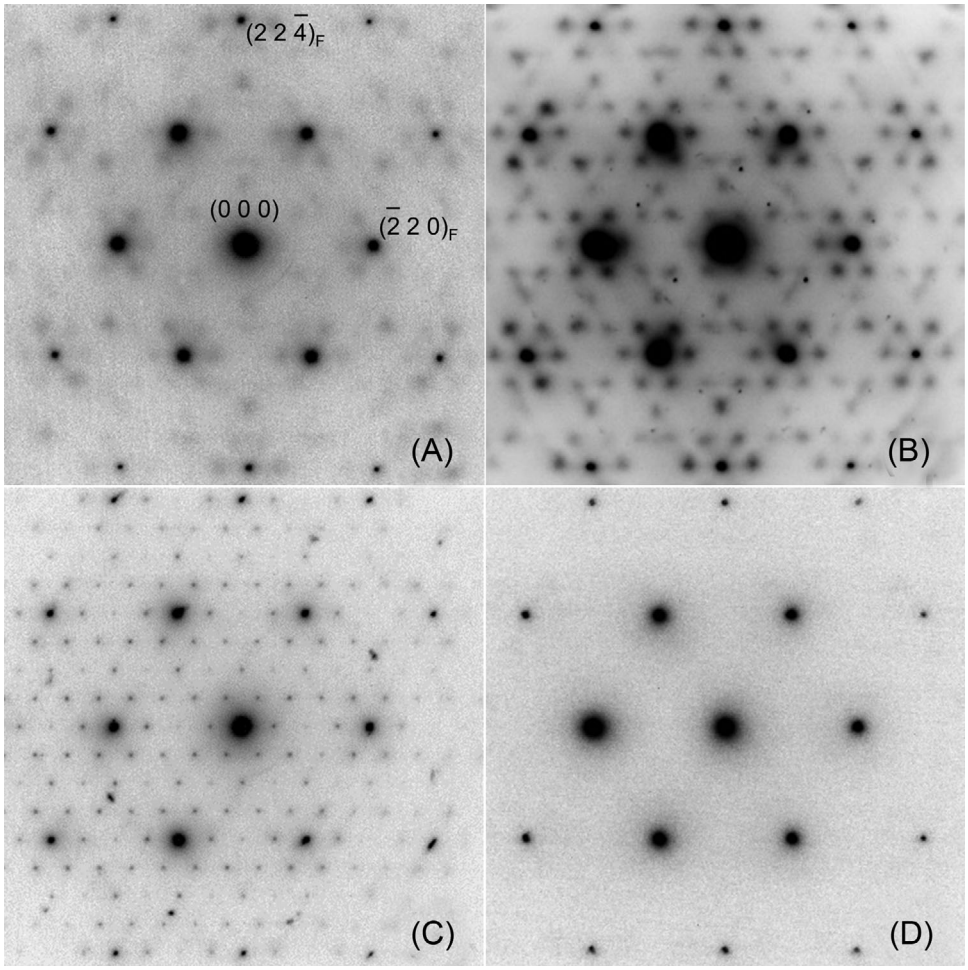

FIGURE 6 Selected area electron diffraction (SAED) patterns (inverted intensity) of the Ln_2ZrO_5 (Ln = Sm, Eu, Gd, and Tb) compounds viewed down zone axis ⟨1 1 1⟩. (A) Sm_2ZrO_5 (diffraction maxima indexed based on the fluorite $Fm\bar{3}m$ symmetry), (B) Eu_2ZrO_5, (C) Gd_2ZrO_5, (D) Tb_2ZrO_5. The brightness and contrast have been altered to enhance and highlight the diffuse diffraction maxima

pyrochlore-defect fluorite compounds that exhibit ⟨110⟩ zone axis patterns similar to those shown in Figure 8G.

The typical electron diffraction patterns for Gd_2ZrO_5 are obtained in four additional zone axis orientations (Figure 7). When observed in the ⟨310⟩ zone axis orientation (Figure 7A), the usual strong diffracted beams are consistent with the parent defect fluorite structure, plus a set of generally weaker, but sharp spots along c* and lying on [00*l*] with *l* odd. Normal to c*, these spots lie on ¼(260)* and thus are commensurate with the lattice. In addition to these spots, there are additional spots, blobs, and streaks of diffuse scattering in this orientation. With regard to the electron scattering in the ⟨411⟩ zone (Figure 7B), the main features include a set of additional sharp spots on ¼(022)* together with additional diffuse blobs and curved diffuse features. The consistent pattern of a quadrupling of the lattice in certain directions is also shown for the ⟨332⟩ zone axis (Figure 7C). In this orientation, we observe sets of sharp diffraction spots indicating a 4x repeat of the fluorite subcell along the three (hhl) reciprocal lattice rows shown in this pattern. The main row of extra spots is interpreted as ¼(220)*. It is noted that the presence of extra rows of spots on each side of and parallel to the main (hhl) rows in this pattern. These rows lead to a pattern of six extra spots around the main beams in each (hhl) reciprocal lattice row; however, the spots in the offset rows are a mix of both sharp and diffuse features. An example of diffuse electron scattering is also presented for the ⟨211⟩ zone axis in Figure 7D. No quadrupling of the lattice was observed in this orientation, which consists mainly of diffuse features located on either side of the ½(113)* reciprocal lattice points, with pairs of short diffuse rods on either side of the ½(111)* coordinates.

3.3 | Ion irradiation

The SAED patterns have been collected in the ⟨110⟩ zone axis orientation for all four samples before and after 1 MeV krypton ion-irradiation (Figure 8). All compositions

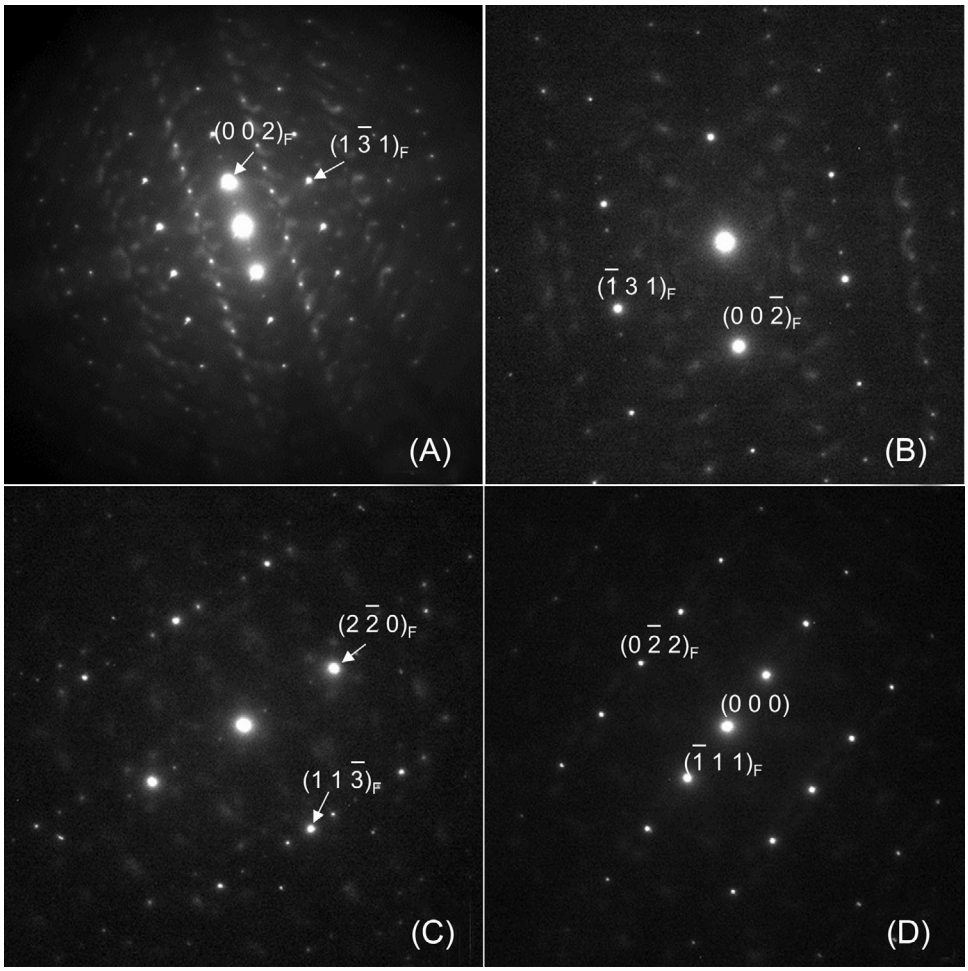

FIGURE 7 Selected area electron diffraction (SAED) patterns taken from various crystal fragments of the Gd_2ZrO_5 compound and are shown down zone axis (A) ⟨310⟩, (B) ⟨411⟩, (C) ⟨332⟩, (D) ⟨211⟩, with two of the diffraction maxima indexed (based on fluorite $Fm\bar{3}m$ symmetry) for each diffraction pattern. The brightness and contrast have been altered to enhance and highlight the diffuse diffraction maxima

show evidence for extra diffraction features on the underlying fluorite lattice, comparing the electron scattering features before and after irradiation. The patterns of the unirradiated samples can be broadly classified as Sm type, Eu–Gd type, and Tb type, the latter pattern being similar to those observed in the "227" defect fluorite compound $Tb_2Zr_2O_7$.[23]

For unirradiated Sm_2ZrO_5 sample, a set of irregularly shaped (star-like) extra diffraction features is observed, which appears to be commensurate with the underlying defect fluorite structure. These are located on or very close to the ½(111)* lattice positions and form rows parallel to c* in the reciprocal lattice (Figure 8A). Following irradiation, this pattern has changed, with weak and slightly incommensurate extra spots now located approximately on 0.27(311)* and "connected" to each other and the strong sublattice spots by diffuse streaks (Figure 8B). These streaks occur along two of the [112] crystallographic directions and form a zigzag pattern parallel to c* in the ⟨110⟩ zone. Figure 8C,D presents the ⟨110⟩ zone axis diffraction patterns for Eu_2ZrO_5 before and after irradiation. Although the image of the unirradiated sample is somewhat grainy, the measured positions of the extra spots lie on ¼(311)* (Figure 8C). The corresponding pattern after irradiation suggests that a similar array of extra spots are retained but are slightly incommensurate with the main lattice, lying on positions related to 0.27(311)*. This also results in a very slight zigzag pattern in the extra spots when traced along c* (e.g., horizontal rows in the pattern shown in Figure 8D). The results for Gd_2ZrO_5 are similar to those of the Eu_2ZrO_5 sample before and after irradiation, with the caveat that the extra spots remain commensurate with the sublattice following the ion irradiation experiment. However, the Gd_2ZrO_5 diffraction patterns (Figure 8E,F) show extra pairs of streaks on both sides of the strong Bragg beams, running parallel to the [111] directions of the reciprocal lattice. The results of the diffraction study on Tb_2ZrO_5 show that the observed scattering from the incommensurate superlattice in the ⟨110⟩ zone is revealed as pairs of weak diffraction spots located on

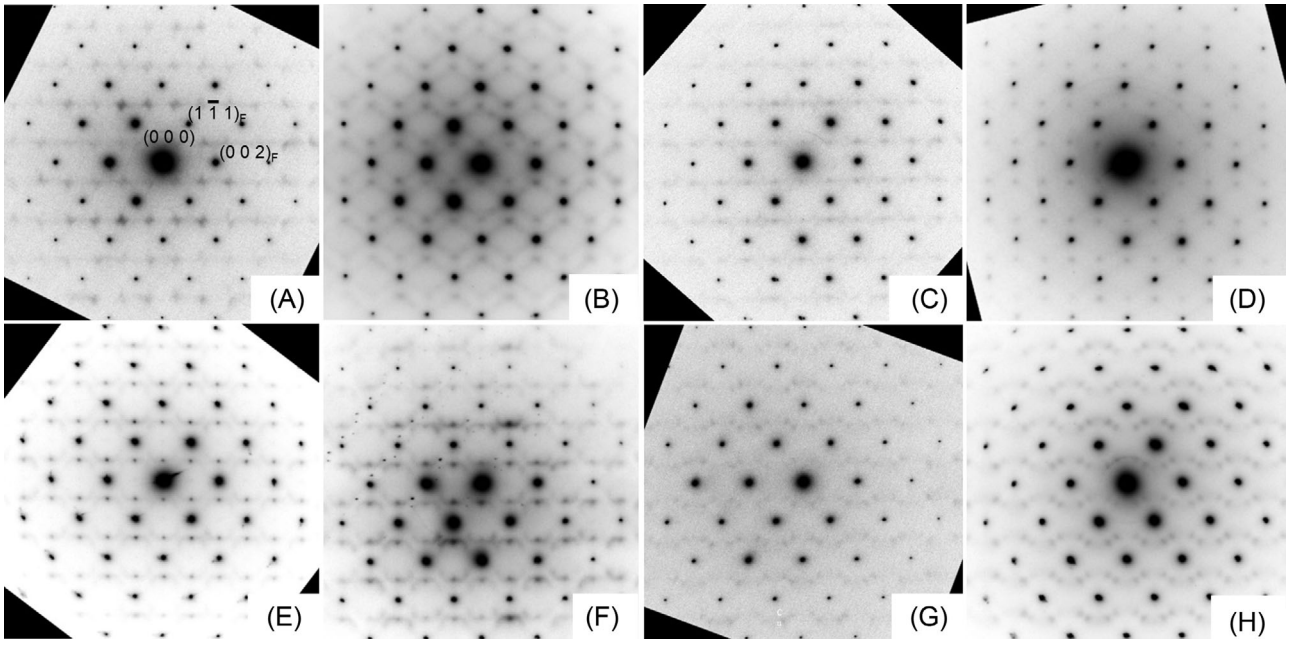

FIGURE 8 Selected area electron diffraction (SAED) patterns (inverted intensity) viewed down zone axis ⟨1 1 0⟩ for pre- (A, C, E, and G) and post- (B, D, F, and H) irradiated (1 MeV krypton ions) for samples (A and B) Sm_2ZrO_5, (C and D) Eu_2ZrO_5, (E and F) Gd_2ZrO_5, (G and H) Tb_2ZrO_5. The brightness and contrast have been altered to enhance the intensity of the diffuse diffraction maxima, and some major fluorite diffraction maxima have been labeled in (A)

either side of 0.5(111)* in the reciprocal space (Figure 8G). The measured distance between the spots is approximately 0.22/(111)* for the unirradiated sample and 0.20/(111)* for the irradiated sample. In general, these results are nearly identical to the observations of Tabira et al.[23] for $Tb_2Zr_2O_7$, indicating that variation of the Tb/Zr/O ratio has had little effect on the nature of the modulations. Previous studies[61,62] have also reported similar diffuse scattering features for several rare-earth zirconates and hafnates in the "227" pyrochlore type stoichiometry, indicating that the observed modulations occur over a range of composition and stoichiometry in these compounds.

Some new electron scattering features have been observed in this series of Ln_2ZrO_5 compounds. The incommensurate structure or modulation is seen to gradually change as the A-site cation radius becomes smaller from Ln = Sm to Tb. For Gd_2ZrO_5, the superstructure is commensurate with the lattice, while for Tb_2ZrO_5, only the strong diffracted beams of the underlying fluorite structure are apparent in the ⟨111⟩ zone axis. However, in the ⟨110⟩ zone, Tb_2ZrO_5 exhibits pairs of extra spots along the (111) plane in a pattern that is nearly identical to that found in a previous study on $Tb_2Zr_2O_7$.[23] In addition, Gd_2ZrO_5 appears to be an ordered superstructure with a fourfold repeat relative to the fluorite subcell. The fourfold repeat is also observed in three other zone axis orientations where it coexists with additional diffuse scattering features. This raises questions about the origin of the scattering, for example, is it entirely due to modulations with some of the scattering at a ¼ value of the fluorite subcell, or could it be due to cation-vacancy ordering? One possibility for the "215" stoichiometry is the development of a Sm–Sm–Zr–vacancy or similar ordering pattern that would be consistent with the fourfold repeat observed in the reciprocal space. This suggestion remains to be determined. Overall, based on the sets of available electron diffraction patterns observed in this study, we can classify the additional scattering observed in the ⟨110⟩ zone axes as Sm type, Eu–Gd type, and Tb type. Following irradiation, we find that the incommensurate superstructure of Sm_2ZrO_5 has changed to the pattern of the Eu-Gd type. To our knowledge, this is the first observation of a change in superstructure in pyrochlore-defect fluorite compounds during irradiation of thin crystals with 1 MeV Kr ions. Generally speaking, these Ln_2ZrO_5 defect-fluorite structures change more or less gradually across the series from Ln = Sm to Tb, with specific superstructures and/or modulations developing as a function of the Ln/Zr cation radius ratio. Under the conditions of our experiments with respect to ion energy, mass, and crystal thickness, it appears that the energy difference between Sm_2ZrO_5 and Eu_2ZrO_5 is the only one that is small enough to be accessible to a measurable change induced by the 1 MeV Kr ion irradiations.

Previous radiation studies on actinide and lanthanide zirconates with the $A_2Zr_2O_7$ stoichiometry have shown

these compounds to be sufficiently radiation-tolerant to avoid any crystalline to amorphous phase transitions. The only exception has been discovered for the amorphization of the $La_2Zr_2O_7$ compound.[16] For $Gd_2Zr_2O_7$, a pyrochlore to fluorite structural change with heavy ion irradiation has been previously shown.[6,20] This pyrochlore to fluorite structural change has also been noted for $Am_2Zr_2O_7$ due to alpha self-irradiation.[3] Our study is the first to look at the irradiation effects in the related defect-fluorite structured zirconates of Ln_2ZrO_5 stoichiometry.

Looking at the previous $Ln_2Zr_2O_7$ ion-irradiation studies, it seemed reasonable to hypothesize that the Ln_2ZrO_5 compounds would maintain their crystalline structure during 1 MeV Kr irradiation. While it was expected that the long-range fluorite structure should be maintained regardless of ion fluence, it has been significant to note that the shorter-range structure, as shown via the diffuse scattering within the electron diffraction patterns, has also been maintained. The only structure to have been altered during ion-irradiation appears to be for the Sm_2ZrO_5 compound. While the fluorite structure remains, the diffuse diffraction maxima from the modulated structure have been subtly changed to something more closely representing that found for the Eu_2ZrO_5 and Gd_2ZrO_5 compounds. This may represent a more stable, lower energy structural configuration for the Ln_2ZrO_5 compounds, although a more in-depth study of the structure and energetics of this system would be required to confirm this. The minimal structural change postirradiation found for the Ln_2ZrO_5 system of compounds lends further evidence of the zirconates tolerance to radiation damage. The maintaining of crystal structure will minimize any volume swelling effects, along with any structural degradation often associated with crystalline to amorphous or crystalline to crystalline phase transitions.

4 | CONCLUSIONS

The use of a soft-chemistry fabrication method has provided complete mixing of the precursors producing homogeneous distribution of elements within the sintered ceramics. This approach has also allowed a relatively low sintering temperature, 1400°C, to be used while still achieving complete reaction between the precursors. This is significant as zirconates tend to be highly refractory and require high sintering temperatures and long sintering times to achieve complete precursor reaction.

The combination of diffraction characterization techniques has given insight into the crystal structure details for the Ln_2ZrO_5 compounds. X-ray and neutron diffraction show that the general structure is well defined by $Fm\bar{3}m$ symmetry. The neutron diffraction data for Tb_2ZrO_5 did indicate a small variation from the expected oxygen vacancies with a slightly higher occupancy noted. However, electron diffraction shows a much more complex structure than just the fluorite-type, something noted in a previous study.[22]

As with previous ion-irradiation studies on rare-earth zirconates, the ion-irradiation response for the newly measured Ln_2ZrO_5 (Ln = Sm, Eu, Gd, and Tb) compounds shows these to be radiation tolerant. The original crystal structure, both long-range fluorite and shorter-range modulations, was maintained up to high fluence using 1 MeV krypton ions.

ACKNOWLEDGMENTS

We sincerely thank Tim Palmer for SEM specimen preparation. Some work was undertaken on the powder diffraction beamline at the Australian Synchrotron with the assistance of Helen Brand. The in situ TEM ion-irradiation study was supported by Meimei Li, Wei-Ying Chen, Pete Baldo, and Ed Ryan at the IVEM Tandem Facility (Argonne National Laboratory), with Office of Nuclear Energy under DOE Idaho Operations Office Contract DE-AC07- 051D14517 as part of a Nuclear Science User Facilities experiment.

CONFLICT OF INTEREST

The authors declare no competing financial interests.

ORCID

Robert D. Aughterson https://orcid.org/0000-0002-1704-024X
Gregory R. Lumpkin https://orcid.org/0000-0002-9266-0457
Zhaoming Zhang https://orcid.org/0000-0003-3273-8889
Linggen Kong https://orcid.org/0000-0001-9518-6802

REFERENCES

1. Malachevsky MT, Rodríguez Salvador D, Leiva S, D'Ovidio CA. Cubic phases in the Gd_2O_3-ZrO_2 and Dy_2O_3-TiO_2 systems for nuclear industry applications. J Ceram. 2015;2015: 298690.
2. Hood J, Akbari F, He Z, Reid P, Corcoran EC & Lewis BJ et al. Zirconia-rare earth oxide phase stability program in support of ACR-1000 fuel design. In: 29th Annual CNS Conference and 32nd CNS /CNA Student Conference; 1–4 June 2008; Toronto, Canada.
3. Martin PM, Belin RC, Valenza PJ, Scheinost AC. EXAFS study of the structural phase transition in the americium zirconate pyrochlore. J Nucl Mater. 2009;385:126–30.
4. Mandal B, Tyagi AK. Pyrochlores: potential multifunctional materials. Barc Newslett. 2010;313:6–13.

5. Hu Q, Zeng J, Wang L, Shu X, Shao D, Zhang H, et al. Helium ion irradiation effects on neodymium and cerium co-doped $Gd_2Zr_2O_7$ pyrochlore ceramic. J Rare Earths. 2018;36: 398–403.
6. Begg BD, Hess NJ, McCready DE, Thevuthasan S, Weber WJ. Heavy-ion irradiation effects in $Gd_2(Ti_{2-x}Zr_x)O_7$ pyrochlores. J Nucl Mater. 2001;289:188–93.
7. Gregg DJ, Zhang Y, Zhang Z, Karatchevtseva I, Blackford MG, Triani G, et al. Crystal chemistry and structures of uranium-doped gadolinium zirconates. J Nucl Mater. 2013;438: 144–53.
8. Gregg DJ, Zhang Y, Middleburgh SC, Conradson SD, Triani G, Lumpkin GR, et al. The incorporation of plutonium in lanthanum zirconate pyrochlore. J Nucl Mater. 2013;443:444–51.
9. Radhakrishnan AN, Rao PP, Linsa KSM, Deepa M, Koshy P. Influence of disorder-to-order transition on lattice thermal expansion and oxide ion conductivity in $(Ca_xGd_{1-x})_2(Zr_{1-x}M_x)_2O_7$ pyrochlore solid solutions. Dalton Trans. 2011;40:3839–48.
10. van Dijk MP, de Vries KJ, Burggraaf AJ. Oxygen ion and mixed conductivity in compounds with the fluorite and pyrochlore structure. Solid State Ionics. 1983;9:913–9.
11. Shlyakhtina AV, Kolbanev I, Knotko A, Boguslavskii M, Stefanovich SY, Karyagina O, et al. Ionic conductivity of $Ln_{2+x}Zr_{2-x}O_{7-x/2}$ (Ln = Sm-Gd) solid solutions. Inorg Mater. 2005;4:854–63.
12. Wu J, Wei X, Padture N, Klemens PG, Gell M, García E, et al. Low-thermal-conductivity rare-earth zirconates for potential thermal-barrier-coating applications. J Am Ceram Soc. 2002;85:3031–5.
13. Bansal NP, Zhu D. Effects of doping on thermal conductivity of pyrochlore oxides for advanced thermal barrier coatings. Mater Sci Eng A. 2007;459:192–5.
14. Vassen R, Cao X, Tietz F, Basu D, Stöver D. Zirconates as new materials for thermal barrier coatings. J Am Ceram Soc. 2000;83:2023–8.
15. Sattonnay G, Moll S, Thomé L, Decorse C, Legros C, Simon P, et al. Phase transformations induced by high electronic excitation in ion-irradiated $Gd_2(Zr_xTi_{1-x})_2O_7$ pyrochlores. J Appl Phys. 2010;108:103512.
16. Lian J, Zu XT, Kutty KVG, Chen J, Wang LM, Ewing RC. Ion-irradiation-induced amorphization of $La_2Zr_2O_7$ pyrochlore. Phys Rev B. 2002;66:054108.
17. Lutique S, Konings RJM, Rondinella VV, Somers J, Wiss T. The thermal conductivity of $Nd_2Zr_2O_7$ pyrochlore and the thermal behaviour of pyrochlore-based inert matrix fuel. J Alloys Compd. 2003;352:1–5.
18. Lutique S, Staicu D, Konings RJM, Rondinella VV, Somers J, Wiss T. Zirconate pyrochlore as a transmutation target: thermal behaviour and radiation resistance against fission fragment impact. J Nucl Mater. 2003;319:59–64.
19. Kong L, Zhang J, Maeda Y, Blackford MG, Li S, Triani G, et al. Novel synthesis and thermal property analysis of MgO–$Nd_2Zr_2O_7$ composite. Ceram Int. 2016;42:16888–96.
20. Wang SX, Begg BD, Wang LM, Ewing RC, Weber WJ, Kutty KVG. Radiation stability of gadolinium zirconate: a waste form for plutonium disposition. J Mater Res. 1999;14:4470–3.
21. Gschneidner KA Jr, Eyring L. Handbook on the physics and chemistry of rare earths. Amsterdam, The Netherlands: Elsevier Science Ltd; 1986.
22. Withers RL, Thompson JG, Barlow PJ. An electron, and X-ray powder, diffraction study of cubic, fluorite-related phases in various ZrO_2–Ln_2O_3 systems. J Solid State Chem. 1991;94:89–105.
23. Tabira Y, Withers RL, Barry JC, Elcoro L. The strain-driven pyrochlore to "defect fluorite" phase transition in rare earth sesquioxide stabilized cubic zirconias. J Solid State Chem. 2001;159:121–9.
24. Wang C.: Experimental and computational phase studies of the ZrO_2-based systems for thermal barrier coatings. Dissertation, University of Stuttgart, (2006).
25. Newman R, Aughterson RD, Lumpkin GR. Synthesis and structure of novel A_2BO_5 compounds containing A = Y, Yb, Gd, Sm, and La and B = Zr, Ti, and Sn. MRS Adv. 2018;3:1117–22.
26. Gschneidner K Jr, Bunzli J-C, Pecharsky V. Handbook on the physics and chemistry of rare earths. Amsterdam, The Netherlands: Elsevier Science Ltd; 2004.
27. Andrievskaya ER. Phase equilibria in the refractory oxide systems of zirconia, hafnia and yttria with rare-earth oxides. J Eur ceram Soc. 2008;28:2363–88.
28. Lyashenko LP, Shcherbakova LG, Belov DA, Knerel'man EI, Dremova NN. Synthesis and electrical properties of Gd_2MO_5 (M = Zr, Hf). Inorg Mater. 2010;46:1341–7.
29. Aughterson RD, Lumpkin GR, de los Reyes M, Sharma N, Ling CD, Gault B, et al. Crystal structures of orthorhombic, hexagonal, and cubic compounds of the $Sm_{(x)}Yb_{(2-x)}TiO_5$ series. J Solid State Chem. 2014;213:182–92.
30. Aughterson RD, Lumpkin GR, Smith KL, de los Reyes M, Davis J, Avdeev M, et al. The ion-irradiation tolerance of the pyrochlore to fluorite $Ho_{(x)}Yb_{(2-x)}TiO_5$ and Er_2TiO_5 compounds: a TEM comparative study using both in-situ and bulk ex-situ irradiation approaches. J Nucl Mater. 2018;507:316–26.
31. Lau GC, Ueland BG, Dahlberg ML, Freitas RS, Huang Q, Zandbergen HW, et al. Structural disorder and properties of the stuffed pyrochlore Ho_2TiO_5. Phys Rev B. 2007;76:054430.
32. Lau GC, McQueen TM, Huang Q, Zandbergen HW, Cava RJ. Long- and short-range order in stuffed titanate pyrochlores. J Solid State Chem. 2008;181:45–50.
33. Jiang C, Stanek CR, Sickafus KE, Uberuaga BP. First-principles prediction of disordering tendencies in pyrochlore oxides. Phys Rev B. 2009;79:104203.
34. Zhang Z, Middleburgh SC, de los Reyes M, Lumpkin GR, Kennedy BJ, Blanchard PE, et al. Gradual structural evolution from pyrochlore to defect-fluorite in $Y_2Sn_{2-x}Zr_xO_7$: average vs local structure. J Phys Chem C. 2013;117:26740–9.
35. Ciomaga Hatnean M, Decorse C, Lees MR, Petrenko OA, Balakrishnan G. Zirconate pyrochlore frustrated magnets: crystal growth by the floating zone technique. Crystals 2016;6:79.
36. Popov VV, Menushenkov AP, Gaynanov BR, Zubavichus YV, Svetogorov RD, Yastrebtsev AA, et al. Features of formation and evolution of crystal and local structures in nanocrystalline $Ln_2Zr_2O_7$ (A = La-Tb). J Phys Conf Ser. 2017;941:012079.
37. Lumpkin GR, Harvey EJ, Smith KL, Blackford MG & Zaluzec NJ. Radiation tolerance of $A_2Ti_2O_7$ compounds at the cubicmonoclinic boundary. In: 15th Pacific Basin Nuclear Conference, 15–20 October; Sydney; 2006.

38. Lumpkin GR, Whittle KR, Rios S, Trachenko K, Pruneda M, Harvey EJ, et al. Radiation damage in pyrochlore and related compounds. MRS Online Proc Libr. 2006;932:64.1.
39. Lumpkin GR, Pruneda M, Rios S, Smith KL, Trachenko K, Whittle KR, et al. Nature of the chemical bond and prediction of radiation tolerance in pyrochlore and defect fluorite compounds. J Solid State Chem. 2007;180:1512–8.
40. Subramanian MA, Aravamudan G, Subba Rao GV. Oxide pyrochlores - a review. Prog Solid State Chem. 1983;15:55–143.
41. Lian J, Chen J, Wang LM, Ewing RC, Farmer JM, Boatner LA, et al. Radiation-induced amorphization of rare-earth titanate pyrochlores. Phys Rev B. 2003;68:134107.
42. Whittle KR, Blackford MG, Aughterson RD, Lumpkin GR, Zaluzec NJ. Ion irradiation of novel yttrium/ytterbium-based pyrochlores: the effect of disorder. Acta Mater. 2011;59:7530–7.
43. Sickafus KE, Minervini L, Grimes RW, Valdez JA, Ishimaru M, Li F, et al. Radiation tolerance of complex oxides. Science 2000;289:748–51.
44. Sickafus KE, Grimes RW, Valdez JA, Cleave A, Tang M, Ishimaru M, et al. Radiation-induced amorphization resistance and radiation tolerance in structurally related oxides. Nat Mater. 2007;6:217–23.
45. Wallwork KS, Kennedy BJ, Wang D. The high resolution powder diffraction beamline for the Australian Synchrotron. AIP Conf Proc. 2007;879:879–82.
46. Hunter B. Rietica - a visual Rietveld program. IUCr Commission on Powder Diffraction. 1998;Newsletter:number 20.
47. Avdeev M, Hester JR. ECHIDNA: a decade of high-resolution neutron powder diffraction at OPAL. J Appl Crystallogr. 2018;51:1597–604.
48. Cliff G, Lorimer GW. The quantitative analysis of thin specimens. J Microsc. 1975;103:203–7.
49. Kirk MA, Baldo PM, Liu AC, Ryan EA, Birtcher RC, Yao Z, et al. In situ transmission electron microscopy and ion irradiation of ferritic materials. Microsc Res Tech. 2009;72:182–6.
50. Kong L, Karatchevtseva I, Aughterson RD, Davis J, Zhang Y, Lumpkin GR, et al. New pathway for the preparation of pyrochlore $Nd_2Zr_2O_7$ nanoparticles. Ceram Int. 2015;41:7618–25.
51. Schneider CA, Rasband WS, Eliceiri KW. NIH Image to ImageJ: 25 years of image analysis. Nat Methods. 2012;9:671–5.
52. Maram PS, Ushakov SV, Weber JKR, Benmore CJ, Navrotsky A. Probing disorder in pyrochlore oxides using in situ synchrotron diffraction from levitated solids–a thermodynamic perspective. Sci Rep. 2018;8:1–11.
53. Kutty KVG, Rajagopalan S, Mathews CK, Varadaraju UV. Thermal expansion behaviour of some rare earth oxide pyrochlores. Mater Res Bull. 1994;29:759–66.
54. Rouanet A. Zirconium dioxide—lanthanide oxide systems close to the melting point. Rev Int Hautes Temp Refract. 1971;8:161–80.
55. Lopato LM, Andrievskaya ER, Shevchenko AV, Red'ko VP. Phase relations in the ZrO_2-Eu_2O_3 system. Russ J Inorg Chem. 1997;42:1588–91.
56. Pascual C, Duran P. Phase equilibria and ordering in the erbia-zirconia system. J Mater Sci. 1981;16:3067–76.
57. Shevchenko AV, Lopato LM, Kir'yakova IE. Interaction of HfO_2 with Y_2O_3, Ho_2O_3, Er_2O_3, Tm_2O_3, Yb_2O_3 and Lu_2O_3 at high temperatures. Izv Akad Nauk SSSR, Neorg Mater. 1984;20:1991–6.
58. Shevchenko AV, Lopato LM, Nazarenko LV. Systems of HfO_2 with samarium, gadolinium, terbium and dysprosium oxides at high temperatures. Izv Akad Nauk SSSR, Neorg Mater. 1984;20:1862–6.
59. Shevchenko AV, Lopato LM, Zajtseva ZA. Interaction of HfO_2 with lanthanum, praseodymium and neodymium oxides at high temperatures. Izv Akad Nauk SSSR, Neorg Mater. 1984;20:1530–4.
60. Petrova MA, Novikova AS, Grebenshchikov RG. Polymorphism of rare earth titanates of the composition Ln_2TiO_5. Inorg Mater. 1982;18:236.
61. Whittle KR, Cranswick LMD, Redfern SAT, Swainson IP, Lumpkin GR. Lanthanum pyrochlores and the effect of yttrium addition in the systems $La_{2-x}Y_xZr_2O_7$ and $La_{2-x}Y_xHf_2O_7$. J Solid State Chem. 2009;182:442–50.
62. Reid DP, Stennett MC, Hyatt NC. The fluorite related modulated structures of the $Gd_2(Zr_{2-x}Ce_x)O_7$ solid solution: an analogue for Pu disposition. J Solid State Chem. 2012;191:2–9.

SUPPORTING INFORMATION

Additional supporting information may be found in the online version of the article at the publisher's website.

How to cite this article: Aughterson RD, Lumpkin GR, Zhang Z, Avdeev M, Kong L. Crystal chemistry and ion-irradiation resistance of Ln_2ZrO_5 compounds with *Ln* = Sm, Eu, Gd, and Tb. J Am Ceram Soc. 2022;105:3521–3533. https://doi.org/10.1111/jace.18294